Journal of Power Sources 466 (2020) 228211

Contents lists available at ScienceDirect

Journal of Power Sources

journal homepage: www.elsevier.com/locate/jpowsour

High accuracy in-situ direct gas analysis of Li-ion batteries☆

Linxiao Geng [a,*], David L. Wood III [a,b], Samuel A. Lewis Sr. [a], Raynella M. Connatser [a], Mengya Li [a], Charl J. Jafta [a], Ilias Belharouak [a,b,**]

[a] Energy and Transportation Science Division, Oak Ridge National Laboratory, Oak Ridge, TN, 37830, USA
[b] Bredesen Center for Interdisciplinary Research and Graduate Education, University of Tennessee, Knoxville, TN, 37996, USA

HIGHLIGHTS

- High accuracy in-situ MS for gas analysis using direct sampling from pouch cells is proposed.
- Increasing upper cut-off voltage in NMC811/graphite pouch cell will increase CO_2 generation.
- O_2 amount was not significantly promoted by increasing the upper cut-off voltage.

ARTICLE INFO

Keywords:
Lithium ion batteries
Gas generation
NMC Cathodes
NMC811
Safety

ABSTRACT

Cycling of lithium-ion batteries containing Ni-rich NMC cathodes at high voltage involves intense gas generation. From a safety standpoint, it is critical to understand how different gas species respond to changes in upper cut-off voltages. In this manuscript, we introduce a novel experimental set up for real-time analysis of gas generation in prismatic pouch cells. In a typical experiment, a lithium-ion pouch cell is directly connected to a quadruple mass spectrometer using a glass capillary. Pressure difference helps move the generated gases to the mass spectrometer column for full analysis. The gaseous species are probed during both formation cycle and aging cycles in Li-ion pouch cells comprising NMC811 cathodes and graphite anodes. The gases are generated upon the creation of the solid electrolyte interphase on graphite during the first formation charge. Ethylene (C_2H_4) is the major gas generated during formation cycle due to the decomposition of ethylene carbonate. H_2, CH_4, C_2H_6, O_2, CO and CO_2 are also monitored during formation cycle. For the aging cycles, three upper cut-off voltages 4.2, 4.4 and 4.6 V are selected to investigate the impact of upper cut-off voltages on gas generation. Higher upper cut-off voltages do not significantly affect the amount of O_2 measured, as a part of the generated oxygen could have reacted with electrolytes. On the other hand, the generation of CO_2 is found to be very sensitive to upper cut-off voltage. During similar aging cycles, 6167 nmol g_{NMC}^{-1} of CO_2 is generated in 4.6 V cycle, versus 1650 nmol g_{NMC}^{-1} in 4.4 V cycle, versus 91 nmol g_{NMC}^{-1} in 4.2 V cycle.

1. Introduction

Great efforts have been made to increase the energy density of lithium ion batteries to further enhance their market penetration in electric vehicles and grid energy storage applications [1–5]. On the cathode side, layered oxides containing nickel, manganese and cobalt ($LiNi_xMn_yCo_zO_2$, labeled NMCXYZ, $x + y + z = 1$) with $x \geq 0.8$ are the most promising candidates for the next generation of Li-ion batteries [6–8]. In fact, some Ni-rich NMC cathodes ($x \geq 0.6$) are already being used in the battery manufacturing industry due to their higher capacities [9]. At the same time, decreasing the Co content is of great benefit due to its high cost and sustainability issues [10,11]. The caveat is that increasing the Ni content in NMC cathodes, such as in NMC811, compromises their chemical and structural stability, causing the batteries to

☆ This manuscript has been authored by UT-Battelle, LLC, under contract DE-AC05-00OR22725 with the US Department of Energy (DOE). The US government retains and the publisher, by accepting the article for publication, acknowledges that the US government retains a nonexclusive, paid-up, irrevocable, worldwide license to publish or reproduce the published form of this manuscript, or allow others to do so, for US government purposes. DOE will provide public access to these results of federally sponsored research in accordance with the DOE Public Access Plan (http://energy.gov/downloads/ doe-public-access-plan).

* Corresponding author.
** Corresponding author. Energy and Transportation Science Division, Oak Ridge National Laboratory, Oak Ridge, TN, 37830, USA.
E-mail addresses: gengl@ornl.gov (L. Geng), belharouaki@ornl.gov (I. Belharouak).

https://doi.org/10.1016/j.jpowsour.2020.228211
Received 7 February 2020; Received in revised form 20 March 2020; Accepted 16 April 2020
Available online 22 May 2020
0378-7753/

fade much faster than the lower Ni content counterparts such as NMC111 [12–16]. Moreover, increasing the upper cut-off voltage in NMC cathodes can further increase energy density, but at the expense of adverse side reactions that occur at the cathode/electrolyte interface, which jeopardizes battery longevity [6,9]. The battery research community has developed methods to investigate these side reactions in cells made of Ni-rich NMC cathodes to better understand them and to develop solutions to reduce their negative impact during high voltage cell operation.

Gas generation is one of the major side reactions during the formation cycling process of lithium ion batteries and their repetitive charge and discharge [17–26]. Gases generated at the electrode/electrolyte interfaces have been reported to cross over between anode and cathode, leading to complex local reactions with other gaseous species, causing even more side reactions at the interfaces [26]. It was also found that gas generation and consumption contribute to materials surface degradation and anode interfacial resistance increase and have a detrimental impact on the long-term cycling of cells [26,27]. Therefore, it has become crucial to probe the gas generation at both the anode/electrolyte and cathode/electrolyte interfaces for understanding of the complex interrelated mechanisms of gas formation. Indeed, the gassing behaviors of NMC cathodes with increased nickel content were investigated using on-line electrochemical mass spectroscopy (OEMS) [22,28,29]. The authors concluded that the higher the nickel content, the lower the onset potential for the gas generation. Particularly, they have attributed the generation of CO_2 and CO to surface oxygen release from NMC cathodes charged at high voltages [29]. Another research group systematically investigated the gassing mechanisms of a NMC622 cathode [30]. By combining ^{18}O isotope labeling and differential electrochemical mass spectroscopy (DEMS), they reported that surface carbonate impurities (such as Li_2CO_3) are the major source for the generation of CO_2 and CO at high voltage [30]. Further studies discussed other mechanisms including decomposition of surface carbonate impurities, surface oxidation of electrolytes and direct electrolyte oxidation as possible triggers for the generation of CO_2 and CO in NMC-based cells [31–33]. The DEMS/OEMS studies provided invaluable insights on the mechanism of gas evolution in Li-ion cells [22–33].

In this paper, we have developed a direct gas sampling technique from pouch cells to a mass spectrometer for analysis of gases generated during cell operation. A lithium-ion pouch cell is directly connected to a quadruple mass spectrometer by a glass capillary. The gases generated move to the mass spectrometer for analysis due to the pressure difference between the two ends of the column. Using this set-up, we have identified a variety of gas species formed in Li-ion pouch cells containing Ni-rich NMC811 cathodes and graphite anodes during both formation cycle and aging cycles. The obtained results clearly demonstrate the robustness and sensitivity of the experimental setup. The effect of upper cut-off voltage and voltage hold during aging cycles on the gassing behavior were probed. We found that increasing the upper cut-off voltage had a direct impact on the amount and composition of gases generated during the aging cycles.

2. Experimental section

2.1. Materials and characterization

Graphite used in this study was purchased from Superior Graphite (product identification SLC 1520T), and the $LiNi_{0.8}Mn_{0.1}Co_{0.1}O_2$ (NMC811) cathode was purchased from Targray with batch number SNMC03008. Polyvinylidene difluoride (PVDF) binders used for anode and cathode slurries were Kureha 9300 and Solvay 5130, respectively, and the carbon black additive Super C65 were purchased from Timcal. N-methyl-2-pyrrolidone (NMP) solvent from Sigma Aldrich was used to make electrode slurries. All materials were used as received without any further treatment and were stored in a dry room with dew point of less than −50 °C (0.1% RH) prior to processing. The electrolyte used in all pouch cells was 1.2 M $LiPF_6$ dissolved in ethylene carbonate and diethyl carbonate (EC/EMC) (3:7 wt%).Water content in the electrolyte was determined to be 4.23 ppm by Karl-Fischer titration. X-ray diffraction (XRD) and scanning electron microscopy (SEM) were used to check the structure and morphology of anode and cathode materials used in this study. The experiments were performed on PANalytical X'Pert Pro MPD and Zeiss Merlin FE-SEM, respectively, and the XRD and SEM data are shown in the supporting information Figs. S1 and S2.

2.2. Li-ion pouch cell assembly

NMC811/graphite pouch cells were fabricated at the U.S. Department of Energy (DOE) Battery Manufacturing R&D Facility (BMF) at Oak Ridge National Laboratory (ORNL). Electrodes were made by coating anode and cathode slurries onto Al and Cu foil current collectors, respectively, using a pilot scale slot die coater (Frontier Industrial Technology). The cathode slurry contained 90 wt% NMC811 powder, 5 wt% carbon black, and 5 wt% PVDF in NMP. The anode slurry contained 92 wt% graphite, 2 wt% carbon black, and 6 wt% PVDF in NMP. The mass loading for the cathode was 11.50 mg cm^{-2} (2.03 mAh cm^{-2}, 2.15 mAh cm^{-2} and 2.27 mAh cm^{-2} at 4.2 V, 4.4 V and 4.6 V upper cut-off voltages, respectively). The mass loading for the anode was 7.45 mg cm^{-2} (2.43 mAh cm^{-2}), yielding a negative to positive capacity ratio (N/P ratio) of 1.20, 1.13 and 1.07 for 4.2 V, 4.4 V and 4.6 V upper cut-off voltages, respectively. After coating and primary drying, all electrodes were calendared to approximately 35% porosity. The electrodes underwent secondary drying at 120 °C in a vacuum oven overnight before being cut and assembled into pouch cells. The electrolyte amount in the pouch cells was 3 times the calculated pore volume of the electrodes and separator. The capacity of the pouch cells was around 420 mAh g^{-1} with 4.2 V upper cut-off voltages. All pouch cell configuration information is summarized in Table 1.

2.3. Pouch cell cycling protocol

For the gassing behavior study during the first formation cycle, the pouch cells were used without any conditioning after cell assembly. During the formation cycle, the pouch cell was charged at C/10 to 4.2 V and then kept at 4.2 V until the current decreased to C/20. The cell was then discharged at C/10 to 3.0 V. For the gassing behavior study during the aging cycles, the same cells that were subjected to gas analysis during the first formation cycle were used. During the aging cycles, the pouch cells were charged at C/3 to the upper cut-off voltages of either 4.2, 4.4 or 4.6 V, followed by voltage holds for 3 h. Thereafter, the cells were discharged to 3.0 V at C/3. All the electrochemical measurements were performed at 30 °C in environmental control chamber.

2.4. In-situ MS measurement set up

For the in-situ MS setup, we developed direct gas sampling from

Table 1
Pouch cell components information.

Component	Composition	Loading (porosity)
Anode	Electrode: 92 wt % SLC 1520T graphite (Superior Graphite, BET surface area 2.07 m^2/g), 2 wt % C65 carbon black (Timcal), 6 wt % PVDF (Kureha); Current collector: Cu foil; Tab: nickel	7.45 mg cm^{-2} (35%)
Cathode	Electrode: 90 wt% $LiNi_{0.8}Mn_{0.1}Co_{0.1}O_2$ (Targray, BET surface area 0.49 m^2/g), 5 wt% C65 carbon black (Timcal), 5 wt% PVDF (Solvay); Size: 48 cm^2; Current collector: Al foil; Tab: aluminum	11.50 mg cm^{-2} (35%)
Separator	Polypropylene–polyethylene– polypropylene (Celgard 2325)	(39%)
Electrolyte	1.2 M $LiPF_6$ in (EC:EMC) (3:7 by wt.%, BASF), 4.23 ppm H_2O from Karl-Fischer Titration	3 × total pore volume

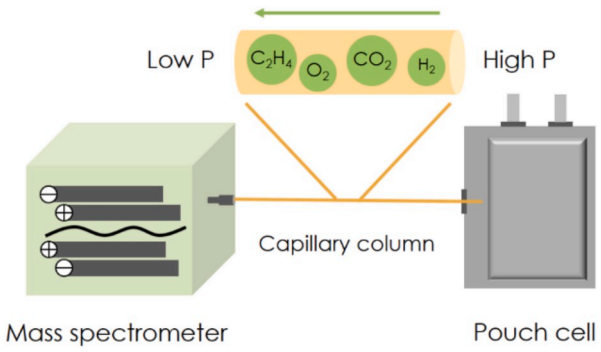

Fig. 1. Schematic of the in-situ MS gas analysis set up.

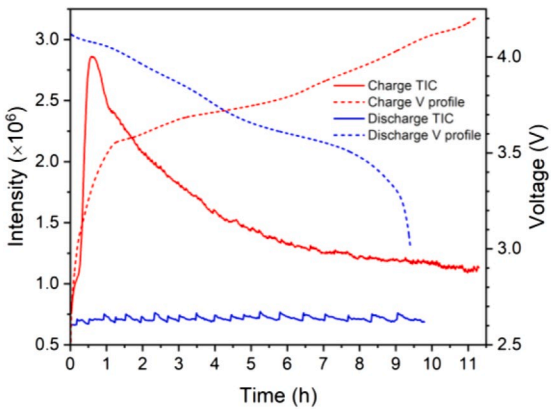

Fig. 2. First formation charge (red dash line) and discharge (blue dash line) curves along with total ion chromatograph (TIC) curves during charging (red solid line) and discharging (blue solid line). (For interpretation of the references to colour in this figure legend, the reader is referred to the Web version of this article.)

pouch cells, and a schematic is shown in Fig. 1, where a commercially available GC-MS instrument (Shimadzu GCMS-QP2020 NX) was used. A glass capillary tube (Polymicro 1068150019) without any stationary phase on the inner wall was first sealed in the pouch cell using hot melt adhesive, and then the other end of the capillary tube was connected to the MS. The length of the capillary tube was determined to be 115 cm, which ensured both optimal accuracy and sensitivity. A pressure of 5 psi was applied on the pouch cells during electrochemical testing. The MS operating parameters are summarized in the supporting information Table S1. The experimental setup developed in this paper has several advantages: (1) common pouch cells are used instead of customized electrochemical cells; (2) practical cell configurations can be used to better assess the gas behavior; and (3) no carrier gas is used, thus maximizing the sensitivity of testing and preventing electrolytes from drying.

3. Results and discussion

3.1. Gas generation during first formation cycle

It is well known that SEI layer forms on the graphite anode mainly during the first few formation cycles. A major part of the of the multiple reaction processes is commonly agreed upon to be the reduction of ethylene carbonate (EC) on the anode surface simultaneously forming polymeric species and generating ethylene gas [34,35]. In this study, we re-examined this complex process with the in-situ setup. For the MS data acquisition, a m/z scan ranging from 2 to 100 was obtained every 30 s. Since only a glass capillary tube was used, all the gaseous species could be drawn into the ultra-high vacuum MS chamber and then analyzed indistinguishably. Total ion chromatographs (TICs) were then acquired, which involves an integration of the full selected m/z range. Specific m/z information can be extracted from TICs for further analysis. The charge-discharge curve along with the real time TIC curve are plotted together in Fig. 2. As seen in the figure, there is a distinct signal spike at the early stage of the first formation charge, which is caused by the anode SEI formation process, and the time of the SEI formation process is in good agreement with previous findings [36]. To help analyze the data from in-situ measurement, a separate ex-situ GC-MS experiment was performed on gases from pouch cells after SEI formation cycling. The gas samples were drawn from pouch cell with gas-tight syringe and injected in the GC-MS. Ex-situ GC-MS analysis complements the in-situ MS gas analysis described in this manuscript because it can separate and identify all the gas species. The qualitative analysis of gases from pouch cell after formation cycling using ex-situ GC-MS is shown in Fig. S3. This process is crucial because due to the real time analysis feature of the in-situ MS setup, the gases were not separated, and all the m/z signals were integrated together. From ex-situ GC-MS experiments, the main species that was found to be generated during cell formation was ethylene (C_2H_4) with contributions from methane (CH_4), carbon dioxide (CO_2), ethane (C_2H_6), etc. In order to extract and quantify the specific m/z for a certain gas, a proper mathematical model was developed. For example, C_2H_4 and CO both have a major fragment of $m/z = 28$. However, C_2H_4 also has a fragment of $m/z = 27$ that is not shared with CO, so C_2H_4 was quantified based on $m/z = 27$. In addition, the contribution of C_2H_4 to $m/z = 28$ was removed for the quantification of CO. Before the data can be analyzed, a library of possible gaseous species that contribute to the TIC must be established first. H_2, CH_4, C_2H_4, C_2H_6, O_2, CO, CO_2 and EMC are hypothesized to make most of the contributions to the TIC during formation cycling and aging. EC makes a negligible contribution to the TIC at room temperature due to its high boiling point. To prove that, a control in-situ MS experiment was conducted with only electrolyte sealed in the pouch, and the signature fragments of EC were found to be negligible. These results can be found in the supporting information Fig. S4. H_2 quantification was used based on $m/z = 2$, and m/z values of 16, 27, 30, 32 and 44 were used to quantify the amounts of CH_4, C_2H_4, C_2H_6, O_2 and CO_2, respectively. However, EMC also contributed to the above m/z signals, and for high quality data and accurate quantification, it was important to remove EMC's contributions from these m/z signals. Extracting EMC's contribution was based on its major m/z fragment peak of 45. Since CO does not have a unique m/z peak, $m/z = 28$ was used to quantify the amount of CO after removing the contribution from EMC, CO_2 and C_2H_6. The setup was calibrated for H_2, CH_4, C_2H_4, C_2H_6, O_2, CO and CO_2 using standard gases.

Also, from Fig. 2, no significant gas generation is observed during the formation discharge process. The intensity baseline is mainly from EMC vapor, so only the gases generated during the first formation charge were quantified. These results are presented in Fig. 3, and the amount of C_2H_4 generated along the formation charge voltage curve is shown in Fig. 3a. The reason for separating C_2H_4 from all other gases is because the amount of C_2H_4 generated is much greater than other gases as is seen in Fig. 3c. This finding is in agreement with the literature that C_2H_4 is the main gas product formed during the first formation cycle as EC from the electrolyte decomposes to generate C_2H_4 and form the organic portion of the SEI [37]. From Fig. 3a and c we can see that almost all the gases are generated within the first 1 h of the formation *charging*. If we compare the gas peaks with the voltage profile, the gas generation process happens during the voltage slope below about 3.5 V. This initial slope is not found in half cells where lithium metal serves as the anode [9]. Moreover, if the slope below 3.5 V along with the gas peaks plotted in Fig. 3b and d is more carefully examined, two slopes make up the voltage profile under 3.5 V. The first voltage slope ranges from around 2.5 V–3.0 V, and the second voltage slope ranges from around 3.0 V–3.5 V. It is important to note that these values all refer to the full cell voltage, and in a full cell, the initial cell voltage in the first formation cycle is much more affected

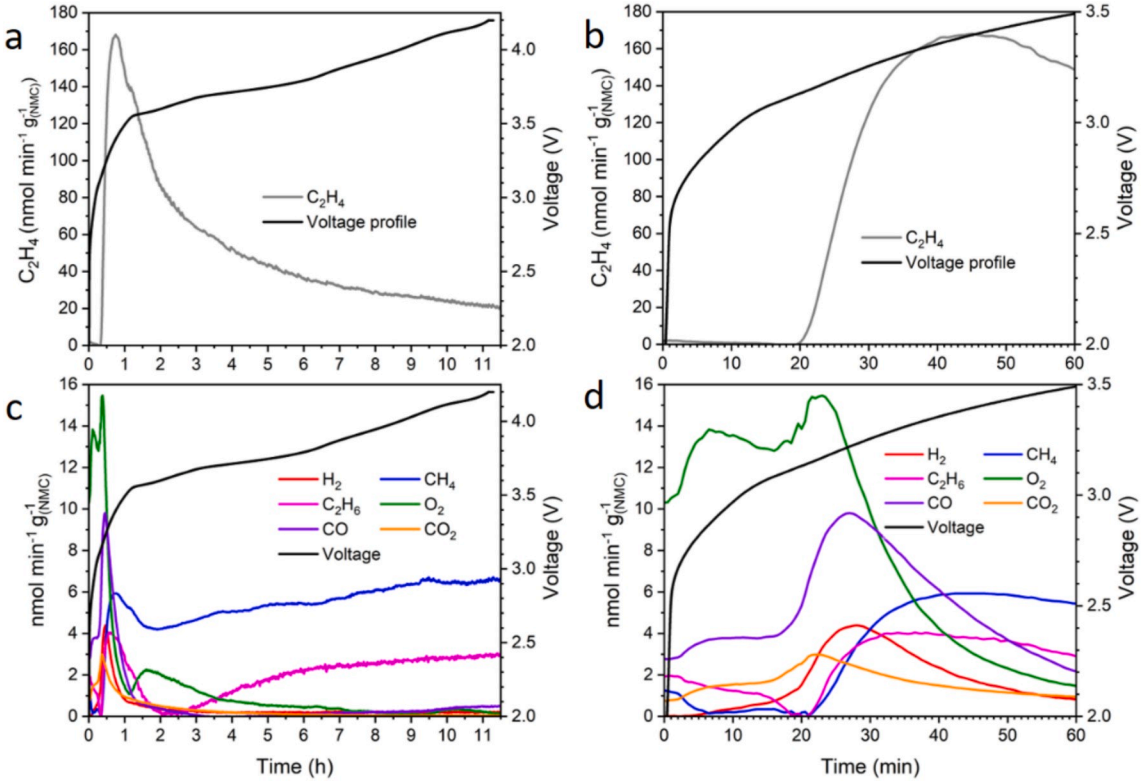

Fig. 3. (a) Ethylene (C_2H_4) generation rate curve along with voltage profile during first formation charge. (b) C_2H_4 generation curve during the voltage range of 2.0 V–3.5 V during the first formation charge. (c) H_2, CH_4, C_2H_6, O_2, CO and CO_2 curve along with voltage profile during first formation charge. (d) A detailed view of the gases from (c) during the voltage range of 2.0 V–3.5 V.

by the anode potential. Interestingly, the trends of the formed gases correlate with the two voltage slopes well. Based on the trends of the gases, we can categorize them during the SEI formation process into two groups: O_2, H_2, CO and CO_2 as one group, and CH_4, C_2H_4 and C_2H_6 as the other group. O_2 has two peaks during SEI formation. The first peak starts early between the first voltage slope from 2.5 V to 3.0 V, and the second O_2 peak starts at the end of the first slope or the beginning of the second slope. The appearance of O_2 generation at such a low potential is very interesting as the oxidation of water generating O_2 is generally believed to happen at high potentials. We hypothesize that the generation of O_2 came from the decomposition of impurities on active material surface or in electrolyte. H_2 has been well investigated and reduction of residue moisture inside the battery is believed to be the main reason [19,38]. The hydrogen evolution reaction (HER) is shown in Equation (1). Reduction of electrolyte solvent contributed to the generation of CO and CO_2, which is displayed in Equations (2) and (3) [23,27,35].

$$2H_2O + 2e^- \rightarrow H_2\uparrow + 2OH^- \quad (1)$$

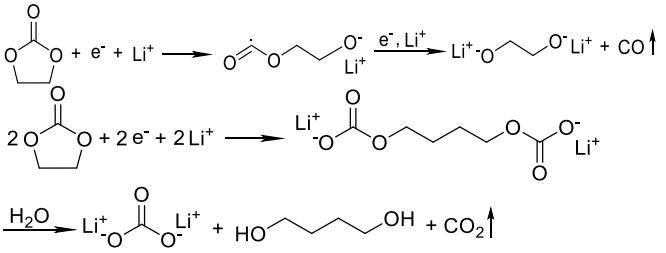

(2)

(3)

Within the second slope around 3.0 V–3.5 V, hydrocarbons including CH_4, C_2H_4 and C_2H_6 started to form. The generation of hydrocarbons is believed to be caused by the reduction of electrolyte solvents on the anode side as the graphite potential continued to drop. It is important to note that the amounts of these hydrocarbons are different from each other; C_2H_4 had a maximum generation rate of about 160 nmol min^{-1} g^{-1} while the peak generation rate of CH_4 and C_2H_6 were about 5 nmol min^{-1} g^{-1}. The generation of C_2H_4 from the reduction of EC is shown in Equation (4) [35,37].

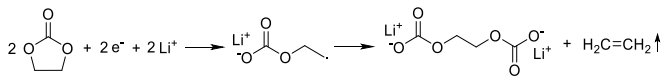

(4)

The generation of CH_4 and C_2H_6 is associated with the reduction of linear carbonate solvents in the electrolyte [23]. To get a better idea of the amount of each gas generated during the first formation charge, the results are summarized in Fig. 4. C_2H_4 accounts for nearly 85% of the gases generated during the first formation charge, and CH_4 and C_2H_6 are the second and third most generated gases. Other literatures has shown that the residual water level has great impact on the cell performance [39–41]. Electrodes that are properly dried should not result in a significant degree of water decomposition during the first formation cycle.

To summarize the gassing phenomena during the SEI formation in the first formation charge, two processes were identified. The first process involves the generation of O_2, H_2, CO and CO_2. The decomposition of residue water, impurities and electrolyte solvent are believed to collectively contribute to the generation of these gases. The second gassing process was much more intense than the first one, and C_2H_4 was the main product caused by the reduction of EC. Saturated hydrocarbons such as CH_4 and C_2H_6 are from the reduction of linear carbonate solvents such as EMC [23,27,35], and C_2H_4 accounted for nearly 85% of all gases during the first formation charge, indicating the reduction of EC is the main source of C_2H_4 as well as formation of the initial portion of the SEI layer.

3.2. Gas generation process at upper cut-off voltage of 4.2 V

Increasing upper cut off voltage effectively increases the initial reversible capacity of NMC811 [9]; however, high upper cut off voltage will also cause the capacity to fade faster. The cycling stability of graphite/NMC full cells with upper cut off voltages of 4.2 V and 4.4 V are compared in Supporting Information Fig. S5. The full cell with a 4.4 V upper cutoff voltage had a higher initial reversible capacity of 205 mAh g^{-1} compared to 195 mAh g^{-1} for the cell with a 4.2 V upper cut off voltage. After 35 cycles, the available capacity of cells with a 4.4 V upper cut off voltage was lower than those with 4.2 V. Over the last several years, a great deal of research has focused on the cause of capacity fade of Ni-rich NMC cathodes with high upper cut off voltages. Reasons such as gas generation, internal cracking, transition metal dissolution, and surface rock-salt reconstruction have been proposed [42–46]. However, a comprehensive study of real time gas generation has not been done with large format full pouch cells. It is crucial to establish a library of gases generated with a full cell set up because the "cross-talk" effect is believed to play a critical role in cell performance. Gases generated at the cathode can migrate to the anode and subsequently be consumed and vice versa [26]. In this study, we compared the gas generation in real time using full pouch cells with upper cut-off voltages of 4.2 V, 4.4 V and 4.6 V.

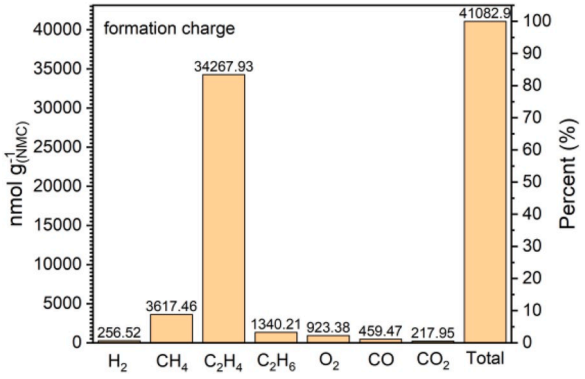

Fig. 4. Total amount of each gas generated during the first formation charge.

The voltage and current profile of an aging cycle using 4.2 V upper cut-off voltage is shown in Figurer 5a, and the generation rate of gases during the aging cycle is plotted with aligned time scale in Fig. 5b. As seen in Fig. 5b, hydrocarbons were the major gases generated during this aging cycle; however, the amount of gases generated were much lower compared to the first formation cycle. C_2H_4 was formed to the greatest extent during the 4.2 V aging cycle, with a peak rate of around 5 nmol min^{-1} g^{-1}. All other gases formed at a rate lower than 2 nmol min^{-1} g^{-1} in throughout the entire cycle. It is hypothesized that the hydrocarbons including CH_4, C_2H_4 and C_2H_4 are from the reduction of electrolyte solvent on the anode side. O_2 and H_2 exhibited discernable trends with changes in voltage., and H_2 is thought to be the product of residual water reduction on the anode side. In terms of the generated O_2, it is well accepted that the lattice oxygen of cathode layered transition metal oxides is released during high voltage operation. However, with a low upper cut off voltage of 4.2 V, very small amount of O_2 was generated during the aging cycle. It also explains why pouch cells with 4.2 V upper

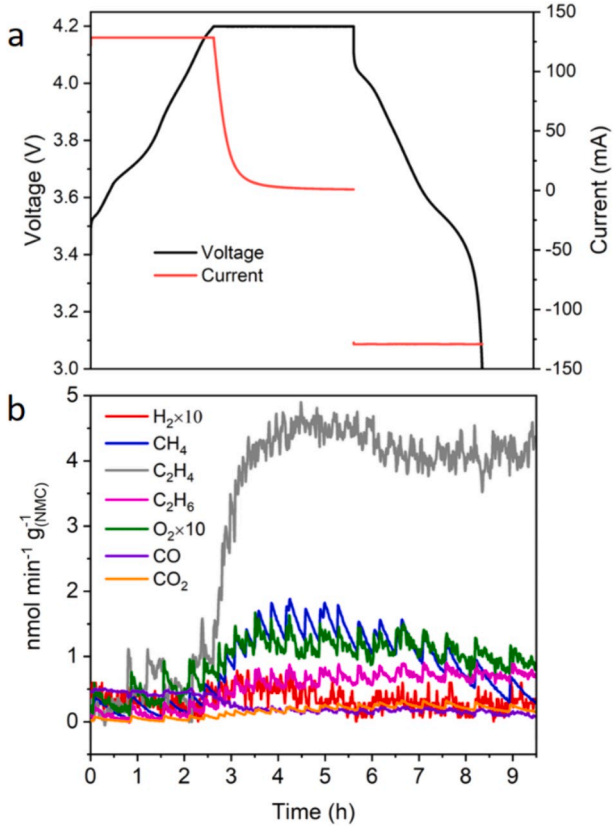

Fig. 5. (a) Charge discharge voltage and current profiles in an aging cycle with upper cut off voltage of 4.2 V. (b) Gas generation curves during 4.2 V aging cycle.

cut-off voltage has a better cycling stability as shown in Fig. S5. It has been reported that CO and CO_2 are oxidation products during high-voltage aging cycles as demonstrated by symmetric cells in a previous study, which is different from the generation mechanism during formation cycling where CO and CO_2 are generated at the anode side [26]. Indeed, with a low upper cut off voltage of 4.2 V, no significant amount of CO or CO_2 was observed. It is worth noting that the onset potential of all the gases generated are similar in the full cell, occurring around 4.2 V, and most of the gases were generated in the upper voltage hold.

3.3. Gas generation process at upper cut-off voltage of 4.4 V

Fig. 6a shows the charge discharge curve along with current profile for a full cell with a 4.4 V upper cut-off voltage. The full cell with 4.4 V upper cut-off voltage has a much greater capacity fading rate than the cell with 4.2 V upper cut-off voltage, making it crucial to investigate the associated differences in gassing behavior. The generation rates of gases during the 4.4 V aging cycle are displayed in Fig. 6b, and the most obvious difference between the two upper cutoff voltages is the amount of CO_2 generated. The CO_2 maximum generation rate was around 6 nmol min^{-1} g_{NMC}^{-1} for the 4.4 V cell as compared to 0.5 nmol min^{-1} g_{NMC}^{-1} for the 4.2 V cell. The total amount of hydrocarbons was found to be lesser for the 4.4 V cycle than for the 4.2 V cycle. It makes sense because the 4.4 V cycle is right after the 4.2 V cycle. SEI layer is more complete over the cycles and thus making the energy barrier of electrolyte solvent decomposition higher. O_2 showed a clear trend in terms of signal change during the 4.4 V aging cycle. Although the amounts of O_2 increased compared to the 4.2 V case, the change was minimal and does not clearly indicate whether lattice oxygen release is much accelerated with a 4.4 V upper cut-off voltage. It is seen in Fig. 6a–b that all the gases shared a similar onset potential of around 4.2 V, indicating these oxidation and reduction processes are related, and maybe even linked to each other [32]. The CO_2 generation mechanism is still debated, and there are three main hypotheses in past research: the first is the surface oxygen is released from the cathode and then chemically oxidizes the electrolyte to form CO_2 [29]; the second is CO_2 from the first cycles are mostly generated from decomposition of surface alkaline residue such as Li_2CO_3 [30]; the third is that the electrolyte is electrochemically oxidized generating CO_2 with the transition metal oxide surface serving as a catalyst [21,47]. Recent studies have demonstrated all three of these proposed mechanisms account for CO_2 generation during high voltage operation [31,32]. From our results, it is clear that CO_2 generation is sensitive to upper cutoff voltage as we compare the results from the 4.2 V and 4.4 V cases, but O_2 generation was not as sensitive. It is hypothesized that upper cut off voltage contributes minimally to the oxygen loss on the transition metal oxide particle surfaces since the quickly formed surface rock salt layer would prevent the oxygen loss from the bulk even if the upper cut off voltage was increased. It must also be pointed out that the generation rate of CO_2 increased even if the process changed from constant high voltage hold to discharging. This phenomenon was also observed in a previous study on NMC622 from the McCloskey group where they saw elevated CO_2 generation rate during open circuit potential hold at high voltage [30]. This phenomenon indicates that the surface carbonate impurities are a significant contributor to the detected CO_2. However, it is also possible that some of the CO_2 gas was either absorbed on the surface or trapped in the pores of materials thus causing a delay in the detection since the concentration of CO_2 generate was at a moderately high rate.

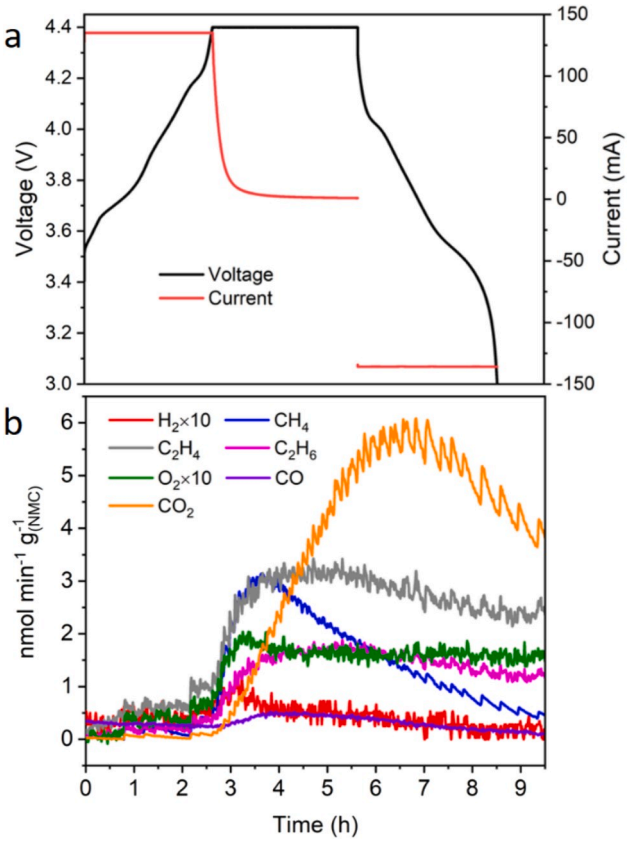

Fig. 6. (a) Charge discharge voltage and current profiles in an aging cycle with upper cut off voltage of 4.4 V. (b) Gas generation curves during 4.4 V aging cycle.

3.4. Gas generation process at upper cut-off voltage of 4.6 V

To shed more light on the effect of upper cut off voltage on the gassing behaviors of the full cell, a more extreme voltage of 4.6 V was implemented. Fig. 7a shows the electrochemical process during the in-situ gas testing, and the charge and discharge capacities were measured at 215 mAh g^{-1} and 211 mAh g^{-1} respectively, an increase of 5.5% compared to the 4.4 V case. Fig. 7b shows gas generation curves for all gases investigated in this study. Since CO_2 dominated the gassing process, the trends of all other gases are displayed in Fig. 7c where they can be seen more clearly. In Fig. 7b, it is observed that all gases were generated around the onset potential of 4.2 V, which is similar to the 4.2 V and 4.4 V cases. CO_2 was found to have a peak rate of around 25 nmol min^{-1} g_{NMC}^{-1}, and its generation rate increased until the last portion of the high voltage hold. For the cell with the 4.6 V upper cut off voltage, however, it is hypothesized that the CO_2 generation was more affected by the decomposition of electrolyte because the generation rate of the CO_2 declined immediately when the battery switched from charge to discharge.

Fig. 7c shows the hydrocarbon generation profiles including CH_4, C_2H_4 and C_2H_6, and they exhibited similar behavior to the 4.2 V and 4.4 V cases. The generation rates of these hydrocarbons gradually decreased compared with previous cycles indicating the completion of SEI layer formation. Interestingly, the O_2 generation level was not significantly increased even with a high upper cut-off voltage of 4.6 V, contradicting the prediction that Ni-rich NMC lattice oxygen is released under high voltage conditions. More detailed study needs to be done to confirm the scale of oxygen release from transition metal oxide lattice.

3.5. Comparison and discussion of gas generation under different upper cut-off voltages

Fig. 8 summarizes the gas amounts generated during the aging cycles with different upper cut-off voltages, where clear trends are seen with regard to cycle number and upper cut-off voltages. For instance, in Fig. 8a it is seen that C_2H_4 accounts for around 60% of all the gases generated followed by CH_4 and C_2H_6. This indicates that electrolyte

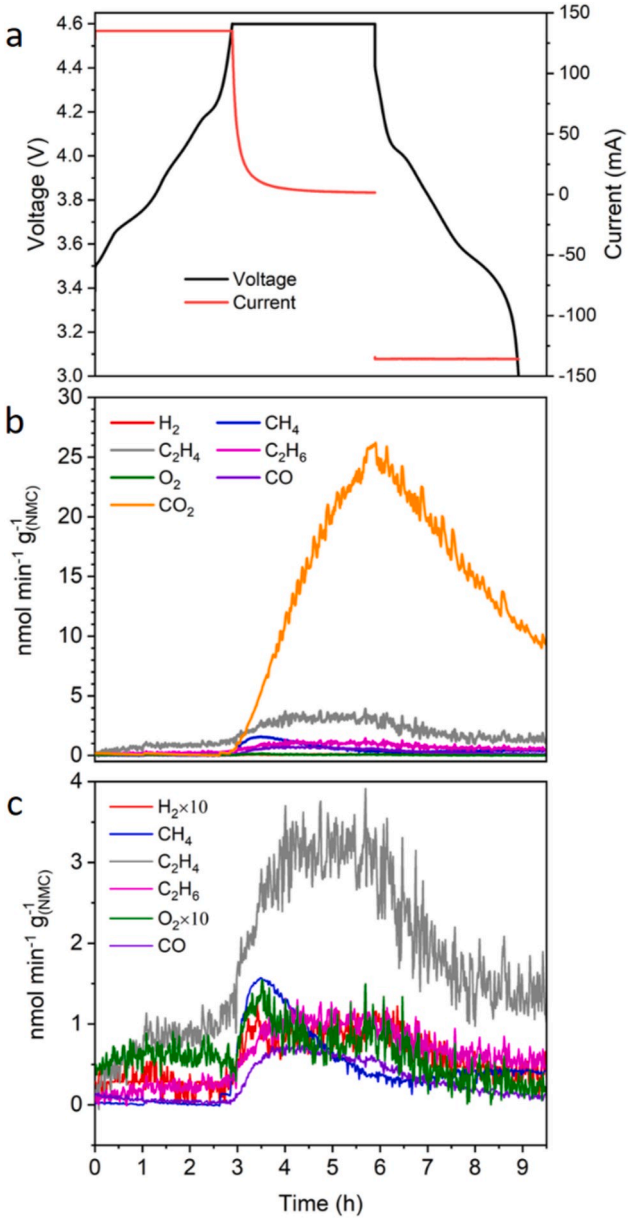

Fig. 7. (a) Charge discharge voltage and current profiles in an aging cycle with upper cut off voltage of 4.6 V. (b) Gas generation curves during 4.6 V aging cycle. (c) Gas generation curves excluding CO_2 during 4.6 V aging cycle.

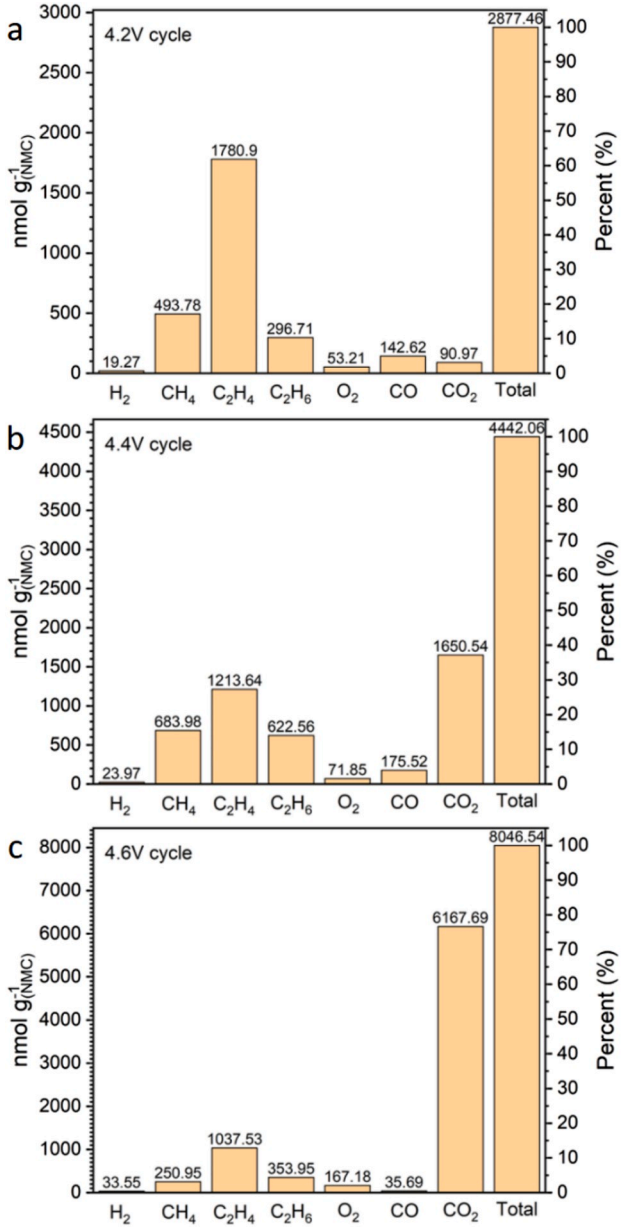

Fig. 8. Gas generation amount in aging cycles with upper cut-off voltages of (a) 4.2 V, (b) 4.4 V and (c) 4.6 V.

solvent continued to be reduced at the anode. These cycles followed the first formation charge-discharge cycle and resulted in a continuation of the anode SEI formation. It is also seen that the amount of gases generated is much less than during formation cycling as the SEI layer becomes thicker and more uniform. The hydrocarbon amounts generated at the anode continued to decrease as the experimental procedure went up to the 4.6 V cycling. The total hydrocarbons decreased from 39226 nmol g^{-1} during the formation cycle to 2571 nmol g^{-1} during the 4.2 V aging cycle to 2520 nmol g^{-1} during the 4.4 V aging cycle to 1642 nmol g^{-1} during the 4.6 V aging cycle. It was also observed that the total amount of hydrocarbons generated in the initial cycles were dependent on the cycle number, but not sensitive to the potential. For the 4.6 V case, the anode was at a more negative potential, but the least hydrocarbons were generated compared to previous cycles with lower upper cut off voltages. As the SEI layer formation completes itself as cycling goes on, less hydrocarbons are generated on the anode side. However, we speculate that the generation of hydrocarbons on the anode side would not come to a complete stop. On one hand, disruptive phenomena such as lithium plating and fast charging is likely to destroy the integrity of the SEI layer at some spots, thus promoting further SEI formation [48–50]. On the other hand, as interfacial resistance goes up and lithium reserve is in short supply, higher overpotential will push the anode to a more negative potential, which will introduce disruptive phenomena and promote the reduction of electrolyte.

Lattice oxygen release from NMC cathodes charged to high voltages has been reported by several research groups [28,29,51–53]. Our experiments also established a clear relationship between oxygen generation amount and upper cut-off voltages, as the O_2 release for the 4.6 V case was 167.18 nmol g^{-1} comparable to 53.32 nmol g^{-1} in 4.2 V case. However, the amount of O_2 was low compared to other gases making it difficult to conclude whether the majority of the O_2 is from layer metal oxide lattice or the decomposition of residual water.

The CO_2 amount, on the other hand, varied substantially as upper cut-off voltage was changed. During the 4.2 V aging cycle, only 90.97 nmol g^{-1} CO_2 was detected, but the amount of CO_2 increased to 1650.54

nmol g^{-1} with a 4.4 V upper cut off voltage. During the 4.6 V cycle, this number further increased to 6167.69 nmol g^{-1}. The trend clearly shows CO_2 generation is highly sensitive to cathode overpotentials. For high voltage cycling, CO_2 generation is the main gassing source. This is in agreement with our previous work on pouch cell gas analysis after extensive cycling [26]. Interestingly, CO generation rates for all three aging cycles were low, which is in contrast to the findings of other researches [29,30]. Even for 4.6 V case, the peak generation rate of CO was below 1 nmol min^{-1} g^{-1}. The presence of C_2H_4, CO_2 and EMC solvent in the system also makes it difficult to accurately quantify the amount of CO. Previous study had used IR technique to accurately quantify the generation of CO during battery operation [38].

The high sensitivity of CO_2 gassing rate to voltage can support both electrolyte oxidation on the NMC811 surface and surface carbonate decomposition. However, the response of CO_2 generation to the voltage and current during 4.4 V and 4.6 V aging cycles showed differences in Figs. 6b and 7b. In Fig. 7b, the CO_2 generation rate immediately dropped as the current flow changed direction. However, there was a lag effect of CO_2 generation to the flow of current in the 4.4 V aging cycle. This subtle difference might provide us valuable insights on the mechanism of CO_2 generation. The direct electrochemical oxidation of electrolyte should be more dependent on the voltage. Combined with the observations from our experiments, moderately high voltage (~4.4 V) promotes similar contributions of CO_2 gassing from both electrolyte oxidation and surface carbonate decomposition in the initial aging cycles, but under high voltage ($\geq$4.6 V), the oxidation of electrolyte should be the major contribution of CO_2. Moreover, the low level of O_2 generation observed made it difficult to reach a conclusion on what the degree of contribution of O_2 was to the generation of CO_2.

4. Conclusion

In this paper, we proposed a novel set up to use mass spectroscopy to directly sample and analyze gases generated in lithium ion pouch cells with NMC811 cathodes. The novel method offers both sensitivity and accuracy in determining the gases generated during both formation cycling and aging cycles. During formation cycling, the anode SEI formation process along with gas generation occurred at the initial stage of the first formation charge. Reduction of EC was demonstrated as the major process with minor residual water associated processes occurring at an even earlier stage. C_2H_4 from the decomposition of EC was the dominating species among the gases generated, accounting for nearly 90% of all the gases generated in the formation cycle. Upper cut-off voltages of 4.2 V, 4.4 V and 4.6 V were selected to investigate the effect of cathode overpotential on the gassing behaviors of the cells during aging cycles. Hydrocarbons generated during the aging cycles were determined to be from the reduction of electrolyte at the anode side as the SEI layer continued towards its full formation. The generation of these hydrocarbons greatly depend on the conditions of SEI layer at the anode side. CO_2 was demonstrated to be highly sensitive to the upper cut-off voltages, with 6167.69 nmol g_{NMC}^{-1} of CO_2 generated during the 4.6 V aging cycle compared to only 90.97 nmol g_{NMC}^{-1} of CO_2 in the 4.2 V aging cycle. On the other hand, O_2 levels were not significantly increased even during the 4.6 V high voltage hold. It is hypothesized that CO_2 is generated at 4.4 V upper cutoff voltage from both electrolyte oxidation and surface carbonate impurity decomposition. At high voltage condition (4.6 V), however, the oxidation of electrolyte is the more dominating process for the CO_2 generation at the cathode.

Declaration of competing interest

The authors declare that they have no known competing financial interests or personal relationships that could have appeared to influence the work reported in this paper.

CRediT authorship contribution statement

Linxiao Geng: Conceptualization, Formal analysis, Investigation, Methodology, Writing - original draft. **David L. Wood:** Supervision, Writing - review & editing. **Samuel A. Lewis:** Methodology. **Raynella M. Connatser:** Methodology. **Mengya Li:** Investigation. **Charl J. Jafta:** Investigation, Writing - review & editing. **Ilias Belharouak:** Supervision, Writing - review & editing.

Acknowledgments

This research at Oak Ridge National Laboratory, managed by UT Battelle, LLC, for the U.S. Department of Energy (DOE) under contract DE-AC05-00OR22725, was sponsored by the Office of Energy Efficiency and Renewable Energy (EERE) Vehicle Technologies Office (VTO) (Program Manager: Peter Faguy). XRD and SEM were conducted at the Center for Nanophase Materials Sciences, which is a DOE Office of Science User Facility.

Appendix A. Supplementary data

Supplementary data to this article can be found online at https://doi.org/10.1016/j.jpowsour.2020.228211.

References

[1] P. Kubiak, Z. Cen, C.M. López, I. Belharouak, J. Power Sources 372 (2017) 16–23.
[2] E. Markevich, G. Salitra, P. Hartmann, J. Kulisch, D. Aurbach, K.-J. Park, C.S. Yoon, Y.-K. Sun, 166 (2019) A5265-A5274.
[3] S.-T. Myung, F. Maglia, K.-J. Park, C.S. Yoon, P. Lamp, S.-J. Kim, Y.-K. Sun, ACS Energy Lett. 2 (2017) 196–223.
[4] P. Rozier, J.M. Tarascon, 162 (2015) A2490-A2499.
[5] N. Nitta, F. Wu, J.T. Lee, G. Yushin, Mater. Today 18 (2015) 252–264.
[6] H.-J. Noh, S. Youn, C.S. Yoon, Y.-K. Sun, J. Power Sources 233 (2013) 121–130.
[7] I. Belharouak, Y.K. Sun, J. Liu, K. Amine, J. Power Sources 123 (2003) 247–252.
[8] N. Zhang, J. Li, H. Li, A. Liu, Q. Huang, L. Ma, Y. Li, J.R. Dahn, Chem. Mater. 30 (2018) 8852–8860.
[9] H.-H. Ryu, K.-J. Park, C.S. Yoon, Y.-K. Sun, Chem. Mater. 30 (2018) 1155–1163.
[10] S. Ahmed, P.A. Nelson, K.G. Gallagher, N. Susarla, D.W. Dees, J. Power Sources 342 (2017) 733–740.
[11] J.R. Croy, B.R. Long, M. Balasubramanian, J. Power Sources 440 (2019) 227113.
[12] S.-M. Bak, E. Hu, Y. Zhou, X. Yu, S.D. Senanayake, S.-J. Cho, K.-B. Kim, K.Y. Chung, X.-Q. Yang, K.-W. Nam, ACS Appl. Mater. Interfaces 6 (2014) 22594–22601.
[13] Y. Mao, X. Wang, S. Xia, K. Zhang, C. Wei, S. Bak, Z. Shadike, X. Liu, Y. Yang, R. Xu, P. Pianetta, S. Ermon, E. Stavitski, K. Zhao, Z. Xu, F. Lin, X.-Q. Yang, E. Hu, Y. Liu, 29 (2019) 1900247.
[14] R. Jung, F. Linsenmann, R. Thomas, J. Wandt, S. Solchenbach, F. Maglia, C. Stinner, M. Tromp, H.A. Gasteiger, 166 (2019) A378-A389.
[15] W. Zhao, J. Zheng, L. Zou, H. Jia, B. Liu, H. Wang, M.H. Engelhard, C. Wang, W. Xu, Y. Yang, J.-G. Zhang, 8 (2018) 1800297.
[16] J. Li, H. Liu, J. Xia, A.R. Cameron, M. Nie, G.A. Botton, J.R. Dahn, 164 (2017) A655-A665.
[17] I. Belharouak, G.M. Koenig, T. Tan, H. Yumoto, N. Ota, K. Amine, J. Electrochem. Soc. 159 (2012) A1165–A1170.
[18] R. Bernhard, M. Metzger, H.A. Gasteiger, 162 (2015) A1984-A1989.
[19] M. Metzger, B. Strehle, S. Solchenbach, H.A. Gasteiger, 163 (2016) A798-A809.
[20] C.P. Aiken, J. Xia, D.Y. Wang, D.A. Stevens, S. Trussler, J.R. Dahn, 161 (2014) A1548-A1554.
[21] K. Kumai, H. Miyashiro, Y. Kobayashi, K. Takei, R. Ishikawa, J. Power Sources 81–82 (1999) 715–719.
[22] R. Jung, M. Metzger, F. Maglia, C. Stinner, H.A. Gasteiger, J. Phys. Chem. Lett. 8 (2017) 4820–4825.
[23] M. Onuki, S. Kinoshita, Y. Sakata, M. Yanagidate, Y. Otake, M. Ue, M. Deguchi, 155 (2008) A794-A797.
[24] G. Gachot, P. Ribière, D. Mathiron, S. Grugeon, M. Armand, J.-B. Leriche, S. Pilard, S. Laruelle, Anal. Chem. 83 (2011) 478–485.
[25] S. Solchenbach, M. Metzger, M. Egawa, H. Beyer, H.A. Gasteiger, 165 (2018) A3022-A3028.
[26] C. Mao, R.E. Ruther, L. Geng, Z. Li, D.N. Leonard, H.M. Meyer, R.L. Sacci 3rd, D. L. Wood 3rd, ACS Appl. Mater. Interfaces 11 (2019) 43235–43243.
[27] L.D. Ellis, J.P. Allen, L.M. Thompson, J.E. Harlow, W.J. Stone, I.G. Hill, J.R. Dahn, 164 (2017) A3518-A3528.
[28] J. Wandt, A.T.S. Freiberg, A. Ogrodnik, H.A. Gasteiger, Mater. Today 21 (2018) 825–833.
[29] R. Jung, M. Metzger, F. Maglia, C. Stinner, H.A. Gasteiger, 164 (2017) A1361-A1377.
[30] S.E. Renfrew, B.D. McCloskey, J. Am. Chem. Soc. 139 (2017) 17853–17860.
[31] S.E. Renfrew, B.D. McCloskey, ACS Appl. Energy Mater. 2 (2019) 3762–3772.

[32] S.E. Renfrew, L.A. Kaufman, B.D. McCloskey, ACS Appl. Mater. Interfaces 11 (2019) 34913–34921.
[33] S.E. Renfrew, B.D. McCloskey, 166 (2019) A2762-A2768.
[34] S. Zhang, M.S. Ding, K. Xu, J. Allen, T.R. Jow, 4 (2001) A206-A208.
[35] S.J. An, J. Li, C. Daniel, D. Mohanty, S. Nagpure, D.L. Wood, Carbon 105 (2016) 52–76.
[36] R. Imhof, P. Novák, 145 (1998) 1081-1087.
[37] M. Nie, D. Chalasani, D.P. Abraham, Y. Chen, A. Bose, B.L. Lucht, J. Phys. Chem. C 117 (2013) 1257–1267.
[38] B.B. Berkes, A. Schiele, H. Sommer, T. Brezesinski, J. Janek, J. Solid State Electrochem. 20 (2016) 2961–2967.
[39] M. Metzger, B. Strehle, S. Solchenbach, H.A. Gasteiger, 163 (2016) A1219-A1225.
[40] R. Jung, R. Morasch, P. Karayaylali, K. Phillips, F. Maglia, C. Stinner, Y. Shao-Horn, H.A. Gasteiger, 165 (2018) A132-A141.
[41] M. Herstedt, D.P. Abraham, J.B. Kerr, K. Edström, Electrochim. Acta 49 (2004) 5097–5110.
[42] J. Zhu, G. Chen, J. Mater. Chem. 7 (2019) 5463–5474.
[43] A. Tornheim, M. He, C.-C. Su, Z. Zhang, 164 (2017) A6366-A6372.
[44] J. Xie, A.D. Sendek, E.D. Cubuk, X. Zhang, Z. Lu, Y. Gong, T. Wu, F. Shi, W. Liu, E. J. Reed, Y. Cui, ACS Nano 11 (2017) 7019–7027.
[45] F. Schipper, H. Bouzaglo, M. Dixit, E.M. Erickson, T. Weigel, M. Talianker, J. Grinblat, L. Burstein, M. Schmidt, J. Lampert, C. Erk, B. Markovsky, D.T. Major, D. Aurbach, 8 (2018) 1701682.
[46] B. Han, T. Paulauskas, B. Key, C. Peebles, J.S. Park, R.F. Klie, J.T. Vaughey, F. Dogan, ACS Appl. Mater. Interfaces 9 (2017) 14769–14778.
[47] K. Leung, J. Phys. Chem. C 116 (2012) 9852–9861.
[48] M. Petzl, M.A. Danzer, J. Power Sources 254 (2014) 80–87.
[49] C. Uhlmann, J. Illig, M. Ender, R. Schuster, E. Ivers-Tiffée, J. Power Sources 279 (2015) 428–438.
[50] B. Wu, J. Lochala, T. Taverne, J. Xiao, Nano Energy 40 (2017) 34–41.
[51] U.H. Kim, D.W. Jun, K.J. Park, Q. Zhang, P. Kaghazchi, D. Aurbach, D.T. Major, G. Goobes, M. Dixit, N. Leifer, C.M. Wang, P. Yan, D. Ahn, K.H. Kim, C.S. Yoon, Y. K. Sun, Energy Environ. Sci. 11 (2018) 1271–1279.
[52] D. Streich, C. Erk, A. Guéguen, P. Müller, F.-F. Chesneau, E.J. Berg, J. Phys. Chem. C 121 (2017) 13481–13486.
[53] A.R. Armstrong, M. Holzapfel, P. Novák, C.S. Johnson, S.-H. Kang, M. M. Thackeray, P.G. Bruce, J. Am. Chem. Soc. 128 (2006) 8694–8698.